INTERNATIONAL JOURNAL FOR NUMERICAL METHODS IN FLUIDS
Int. J. Numer. Meth. Fluids 2013; **73**:344–361
Published online 30 April 2013 in Wiley Online Library (wileyonlinelibrary.com). DOI: 10.1002/fld.3802

Quantitative comparison of Taylor flow simulations based on sharp-interface and diffuse-interface models

S. Aland[1], S. Boden[2], A. Hahn[3], F. Klingbeil[4], M. Weismann[5] and S. Weller[5,*,†]

[1]*Institut für Wissenschaftliches Rechnen, TU Dresden, 01069 Dresden, Germany*
[2]*Helmholtz-Zentrum Dresden-Rossendorf, Bautzner Landstraße 400, 01328 Dresden, Germany*
[3]*Institut für Analysis und Numerik, Universitätsplatz 2, 39106 Magdeburg, Germany*
[4]*University of Erlangen, Applied Mathematics I, Department of Mathematics, Cauerstr. 11, 91058 Erlangen, Germany*
[5]*University of Erlangen, Applied Mathematics III, Department of Mathematics, Cauerstr. 11, 91058 Erlangen, Germany*

SUMMARY

A pressure-driven flow of elongated bullet-shaped bubbles in a narrow channel is known as Taylor flow or bubble-train flow. This process is of relevance in various applications of chemical engineering. In this paper, we describe a typical simplified experimental setting, with surface tension, density and viscosity as prescribed input parameters. We compare a sharp-interface model based on a moving grid aligned with the bubble boundary (ALE coordinates) and a diffuse-interface model where the bubble shape is implicitly given by a phase-field function. Four independent implementations based on the two modeling approaches are introduced and described briefly. Besides the simulation of the bubble shapes, we compare some resulting quantities such as pressure difference and film widths within the implementations and to existing analytical and experimental results. The simulations were conducted in 2D and 3D (rotationally symmetric). Good accordance of the results indicate the applicability and the usability of all approaches. Differences between the models and their implementations are visible but in no contradiction to theoretical results. Copyright © 2013 John Wiley & Sons, Ltd.

Received 31 October 2012; Revised 6 March 2013; Accepted 24 March 2013

KEY WORDS: free surface flow; multiphase flow; finite element method; Taylor bubbles; arbitrary Lagrangian Eulerian method; phase field

1. INTRODUCTION

Taylor bubbles are long bubbles of gas in capillary tubes filled with liquid. Typically, they exhibit a distinct bullet shape with a nearly circular head.

Taylor bubbles were originally described by G. Taylor [1]. In this work, he reports on experiments on the rise of bubbles in nitrobenzene. The bubble volume was comparatively large ($1.5 - 34\ \mathrm{cm}^3$), but later on, Taylor bubbles were also observed in much smaller regimes [2], up to microfluidic experiments.

Taylor flow is usually defined as the flow of a series of elongated bubbles in a narrow channel, where the diameter of the channel is almost entirely filled by the bubbles. It has also been called 'slug flow' or 'bubble-train flow' in literature [2, 3].

In very large diameter tubes, Taylor bubbles do not appear, whereas in small tubes, they are very stable [4]. In contrast to the stable regime of Taylor flow, other types of flows can be observed in capillary channels, depending on gas fraction and velocity [5]:

*Correspondence to: S. Weller, University of Erlangen, Applied Mathematics III, Department of Mathematics, Cauerstr. 11, 91058 Erlangen, Germany.

†E-mail: weller@math.fau.de

Copyright © 2013 John Wiley & Sons, Ltd.

- *Bubbly flow*, which is observed for low gas fractions at moderate velocities, where only few of the bubbles coalesce. In this case, only single small bubbles in a semi-random pattern appear in the fluid.
- *Churn flow*, in similar conditions as Taylor flow, but at higher velocities (i.e., higher Reynolds number). Here, chaotic bubble patterns can be observed. If the fluid velocity is not too high, a mixture of Taylor flow and Churn flow might be observed, where Taylor bubbles are still bullet-shaped at the cap, but show a turbulent flow pattern and a mixture of gas and fluid at the rear [6].
- *Film flow*, happens at high velocities and low liquid fractions, and is characterized by a thin liquid film forming wavy patterns on the channel wall.
- *Annular flow*, which is similar to film flow, but also exhibits a mixture of gas and liquid phases in the core of the channel, and happens at even higher velocities.

It is not always easy to determine in which regime which type of flow will occur. For some situations, so-called flow maps have been constructed, which can predict the kind of flow that can be observed [5]. Often, the kind of injection of gas into the fluid also plays a role.

Many technical applications exist where Taylor flow occurs, for example, in monolith structures that can be found in catalytic converters [7], multiphase monolith reactors [5, 8], or microfluidic channels [9, 10]. In these applications, bubbles of identical size, shape, and distance to each other are typically required. Thus, the hydrodynamics that lead to a perfect bubble-train flow are of interest in these research areas.

In a theoretical investigation on Taylor flow, a relation between the capillary number and the film width between the bubble and the channel wall has been derived [11]. It is approximately valid (with $\leqslant 5\%$ error) for $Ca \leqslant 3 \cdot 10^{-3}$:

$$h_{\mathrm{film}} = \frac{d}{2} \cdot 1.3375 \cdot Ca^{2/3}, \tag{1a}$$

where d denotes the channel diameter. For $0.05 \leqslant Ca \leqslant 100$, a different approach using the boundary element method and numerical simulations leads to the following approximation [12]:

$$h_{\mathrm{film}} = \frac{d}{2} \cdot 0.417 \cdot \left(1 - \exp(-1.69 \cdot Ca^{0.5025})\right). \tag{1b}$$

Although this approach was derived for a pure 2D simulation of Taylor flow, we also used it as an initial guess of film width for our 3D rotational symmetric simulations.

The shape of Taylor bubbles is known to be close to spherical at the cap and the rear, and almost cylindrical in between [11]; however, this is only valid for relatively small capillary numbers. If surface tension effects are less pronounced (higher capillary numbers), Taylor bubbles assume a typical bullet shape, and the cap and rear differ significantly.

In this paper, we simulate Taylor bubbles to examine the effect of varying capillary numbers on the shape of the bubble. Our main focus is on the comparison of different numerical approaches among each other and with experiments. In contrast to other numerical multiphase flow benchmarks (e.g., [13, 14]), we select physical parameters that are very similar to those in experimental setups, and we include sharp-interface and diffuse-interface models. Four independently implemented solvers were used, two using a sharp-interface model, and two a diffuse-interface model.

Because Taylor flow has a stable (quasi-) stationary state, and also high-resolution X-ray measurements are only available on stationary Taylor bubbles, we restrict the comparison to the stationary state (in a moving frame of reference).

The structure of this paper is as follows: we first specify the physical parameters and output parameters of the benchmark (Section 2). Then, we shortly describe the different mathematical models at the core of the four compared solvers (Section 3). The numerical methods of the solvers

Copyright © 2013 John Wiley & Sons, Ltd.

DOI: 10.1002/fld

are also compared (Section 4), and in Section 5, the numerical results are presented. Finally, a short conclusion follows (Section 6).

2. SPECIFICATION OF THE BENCHMARK PROBLEMS

The benchmark consists of three parts:

Problem 1 2D Taylor flow (Bretherton problem) with varying capillary numbers.
Problem 2 3D Taylor flow under the assumption of rotational symmetry with varying capillary numbers.
Problem 3 A single 3D Taylor bubble under the assumption of rotational symmetry, which is compared with experimental data.

For the first two items, the same physical quantities are used, whereas for the third item, all physical parameters are chosen according to the experimental environment.

2.1. Parameters for the purely numerical benchmarks

All parameters in the numerical benchmark (Problems 1 and 2) are chosen similar to [3]. Although these benchmark tests are purely numerical, the physical parameters are selected so that they are close to a experimentally realizable situation (a round capillary of ≈ 1 mm diameter filled with air bubbles in glycerol), see Table I.

A nondimensionalization leads to the dimensionless quantities given in Table II. We chose to vary the capillary number since it is known to be the most important parameter with respect to the shape of the Taylor bubble [3, 11]. Although the capillary number computed from Table I is $2 \cdot 10^{-2}$, we chose to include one simulation with a capillary number a factor of 10 higher, and two capillary numbers a factor of 10 and 100, respectively, lower. These additional simulations have been included to enable a comparison with the approximation formulas (1a) and (1b).

The viscosity and/or density ratios in both fluids are not prescribed, because it is not possible to choose them freely in every method. However, a ratio that is close to the experimental setups (a much lower density and viscosity in the gas phase) is desirable. For glycerol/air, the real ratio is approximately 1:1000 for both density and viscosity.

Table I. Physical parameters for the numerical benchmark (Problems 1 and 2).

ρ_L	$1 \cdot 10^3$	$\frac{kg}{m^3}$	Density of liquid phase
ρ_G	$\ll \rho_L$		Density of gas phase
η_L	$1 \cdot 10^{-2}$	$Pa\,s$	Dynamic viscosity of liquid phase
η_G	$\ll \eta_L$		Dynamic viscosity of gas phase
σ	$5 \cdot 10^{-4}$	$\frac{N}{m}$	Surface tension coefficient
V	$1 \cdot 10^{-3}$	$\frac{m}{s}$	Characteristic velocity
d	$1 \cdot 10^{-3}$	m	Characteristic length, width of computational domain
L	$1 \cdot 10^{-2}$	m	Length of computational domain

Table II. Dimensionless quantities for the numerical benchmark (Problems 1 and 2).

Re_L	$\frac{\rho_L V d}{\eta_L}$	$1 \cdot 10^{-1}$	Reynolds no. in liquid phase
Re_G	$\frac{\rho_G V d}{\eta_G}$	$\approx Re_L$	Reynolds no. in gas phase
Ca	$\frac{\eta_L V}{\sigma}$	$2 \cdot 10^{\{-4,-3,-2,-1\}}$	Capillary no.
We	$Re_L\, Ca$	$1 \cdot 10^{-1} Ca$	Weber no.

Copyright © 2013 John Wiley & Sons, Ltd.

DOI: 10.1002/fld

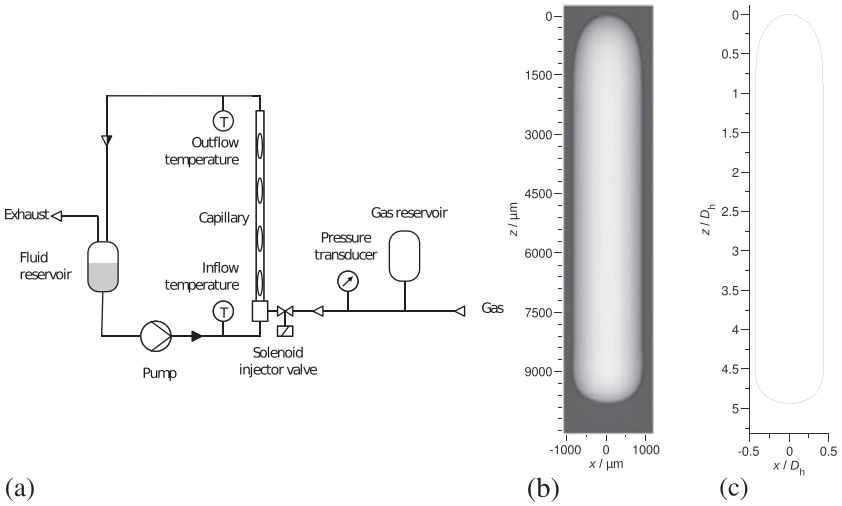

Figure 1. (a) Schematic drawing of the experimental setup. (b) Superimposed X-ray projections of a single Taylor bubble moving in a circular capillary; the capillary structures are removed from the image by subtraction. (c) The extracted projected bubble shape.

2.2. *Experimental setup and discussion for Benchmark 3*

Experimental setup

The experimental setup is schematically depicted in Figure 1 (a). Within a loop, the liquid is pumped through a vertically aligned borosilicate glass capillary of circular cross section with a wall thickness of approximately 0.25 mm. The hydraulic diameter was determined to be 1.98 mm. Pressurized air was injected into the liquid by means of a high-speed injection valve. The valve was attached to the remaining port of the T-junction at the lower end of the capillary tube. The consumed two-phase mixture was fed through a flexible tube at the top of the capillary back to the liquid container. There, the gas is separated from the liquid. By controlling pump power and inlet tube resistance, the fluid velocity was varied. Then, by changing the duty cycle of the valve, the specific Taylor bubble flow regime was produced. The temperatures of the fluid were measured at the entrance and the exit of the capillary. The visualization experiments were conducted at the synchrotron radiation source ANKA. White X-ray radiation provided at the TOPO/TOMO beamline [15] was used to project a 1.78 mm $\times$ 2.31 mm wide portion of the capillary onto a fast X-ray image detector. The detectors' high-speed camera was read out at frame rates up to 36,000 frames per second.

Data processing

Image processing algorithms were used to extract bubble shape information from the images. Because the recorded images only show part of the bubble because of the restricted field of view, a visualization of the whole bubble was created by superposition of consecutive raw X-ray images. The bubble's instantaneous velocity was measured by following their tip positions as the bubble moves through the field of view. A careful analysis of the image brightness distribution at the edge of the projected bubble was performed and thus the projected liquid film thickness, that is the distance between the bubble's interface and the channel's edge, was obtained.

Results

An aqueous solution of 76.9% glycerol (Sigma Aldrich 49770) and 23.1% deionized water was used as liquid. The average temperature at the position where the X-ray beam impinges the capillary was estimated to be 27.1°C. By using tabulated values for density, surface tension and viscosity [16], the capillary and Reynolds number were determined to be $Ca = 0.093$ and $Re = 16.7$. Because the total capture time of the high-speed camera was limited to only a few seconds for the chosen frame rate of 36,000 frames per second, only two bubbles were captured during the experimental run,

Copyright © 2013 John Wiley & Sons, Ltd.

DOI: 10.1002/fld

Table III. Physical parameters for the benchmark (Problem 3).

ρ_L	$1.196 \cdot 10^3$	$\frac{kg}{m^3}$	Density of liquid phase, literature data fit
ρ_G	$\ll \rho_L$		Density of gas phase
η_L	$29.8 \cdot 10^{-3}$	$Pa\,s$	Dynamic viscosity of liquid phase, literature data fit
η_G	$\ll \eta_L$		Dynamic viscosity of gas phase
σ	$66.8 \cdot 10^{-3}$	$\frac{N}{m}$	Surface tension coefficient, literature data fit
V	$210.2 \cdot 10^{-3}$	$\frac{m}{s}$	Bubble velocity, measured in experiment
d	$1.98 \cdot 10^{-3}$	m	Hydraulic diameter, measured in radiographic projection
A	$20.68 \cdot 10^{-9}$	m^3	Bubble volume, computed from 2D bubble shape measured in radiographic projection
L	$1 \cdot 10^{-2}$	m	Length of computational domain

Table IV. Dimensionless quantities for the experimental benchmark (Problem 3).

Re_L	$\frac{\rho_L V d}{\eta_L}$	$1.67379 \cdot 10^1$	Reynolds no. in liquid phase
Re_G	$\frac{\rho_G V d}{\eta_G}$	$\approx Re_L$	Reynolds no. in gas phase
Ca	$\frac{\eta_L V}{\sigma}$	$9.39637 \cdot 10^{-2}$	Capillary no.
We	$Re_L\, Ca$	$1.57275 \cdot 10^0$	Weber no.

of whose only one bubble is considered here. Also, the imaging window height was substantially shorter than the observed bubble. Figure 1(b) shows a superimposed image of the Taylor bubble as a result from all X-ray images of that single bubble superimposed at their calculated positions and after subtracting the structures of the glass capillary from the picture. The bubble velocity was measured to be 210.63 mm/s at the moment as it passed the X-ray beam, the length of the bubble was 9.8 mm. Figure 1(c) shows the bubble's contour as it was determined from Figure 1(b) with subpixel resolution at the edge of the bubble where the image brightness crosses the background intensity level. Assuming axial symmetry, the bubble's volume was measured from its shape to be 20.7 mm^3.

The physical parameters can be found in Table III. A nondimensionalization leads to the dimensionless quantities given in Table IV.

Discussion

Data from other experimental runs confirmed that the bubble velocity fluctuated by 0.7%, and the bubble length fluctuated by 1.5%, each from bubble to bubble. However, the observed shapes at the front and the rear did not vary between each other by more than 0.1% with respect to the hydraulic diameter. This gives confidence in the reported results. Moreover, the accuracies of calculated capillary and Reynolds number are dictated mostly by the variance in viscosity, which is a function of the liquid's temperature. Temperature measurements of the liquid at the inlet and the outlet of the capillary were done at a precision of ± 0.5 K, which in turn causes the uncertainties of Ca and Re_L to be 3.5%. Additional 0.5% uncertainty in these values resulted from the limited detector resolution of 5 μm. The radiographic projections show because of the highly redundant data without any doubt superior image quality and are thus privileged to serve as reference for bubble shape measurements here.

2.3. Initial bubble shape

In all simulations, we fixed the form of the initial bubble shape (see Figure 2). It is chosen as two half-circles connected by straight edges. The initial total length of the bubble is 5 times the hydraulic diameter and the initial film width is chosen according to (1a) for $Ca < 0.05$ or (1b) otherwise.

Copyright © 2013 John Wiley & Sons, Ltd.

DOI: 10.1002/fld

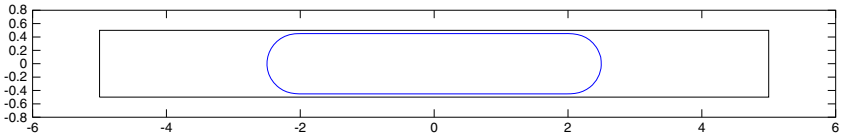

Figure 2. Initial bubble shape. The computational domain is rotated by 90 degrees.

For Benchmark 3, the bubble length was chosen as in the experiment (cf. Table III), and the film width such that the bubble volume fitted the experimental data.

The bubble was placed in a domain of size 1×10 (in multiples of the characteristic length from Table I). The boundary condition for the fluid was chosen as no-slip (Dirichlet) at the sides, and periodic in flow direction (so that a train of bubbles is simulated).

The fluid was driven by an external pressure difference Δp, which is the difference in pressure between the inflow and outflow domain boundary. The magnitude of this external pressure difference is *a priori* unknown and has to be adapted during the simulation to achieve the desired bubble velocity V of Table I, and the simulation reaches a stationary state.

2.4. Output parameters

The output parameters of the numerical benchmark (Problems 1 and 2) were defined as follows:

1. The pressure difference Δp needed to reach the required bubble velocity.
2. The velocity profile of the slug, that is, the liquid phase, at a cut in x-direction directly at the rear of the bubble. This position was chosen because the most interesting flow phenomena happen in the wake of the bubble.
3. The bubble shape – this includes the shape of the head and tail of the bubble as well as the film thickness over the length of the bubble. The film thickness is of special interest because approximation formulas exist in literature, that is, (1a),(1b).

For the comparison to experimental data (Problem 3), only the bubble shape was available from experimental measurements.

3. MATHEMATICAL MODEL

3.1. Sharp-interface model

We consider the Navier–Stokes equations on a time-dependent, *a priori* unknown domain $\Omega = \Omega(t) \subset \mathbb{R}^2$, with a jump condition on a phase boundary Γ:

$$\rho_r(\partial_t \mathbf{u} + \mathbf{u} \cdot \nabla \mathbf{u}) - \nabla \cdot \mathbf{S}(\mathbf{u}, p) = 0 \quad \text{in } \Omega, \tag{2a}$$

$$\nabla \cdot \mathbf{u} = 0 \quad \text{in } \Omega, \tag{2b}$$

$$[\![\mathbf{Sn}]\!]_\Gamma = \frac{1}{We}\kappa \mathbf{n} \quad \text{on } \Gamma. \tag{2c}$$

Here, $\mathbf{S} = \mathbf{S}(\mathbf{u}, p) = \frac{1}{Re}(\nabla \mathbf{u} + (\nabla \mathbf{u})^\top) - pI$ is the stress tensor, Re is the piecewise constant Reynolds number, $Re = Re_L$ in the liquid domain and $Re = Re_G$ in the gaseous domain, We is the Weber number, ρ_r is the ratio of densities, and $\mathbf{n}$ is the unit normal vector on the phase boundary Γ. $[\![\cdot]\!]_\Gamma$ describes the jump over the phase boundary.

In the sharp-interface model, the phase boundary Γ is treated as a $(d-1)$-dimensional manifold in $\mathbb{R}^d$, $d = 2, 3$ (in contrast to phase-field models).

Because the density and the viscosity ratios are very high, we neglect the effects of the gas phase (except in surface tension), and replace Equation (2c) by the following equation:

$$\mathbf{Sn} = \frac{1}{We}\kappa \mathbf{n} \text{ on } \Gamma. \tag{2d}$$

Copyright © 2013 John Wiley & Sons, Ltd.

DOI: 10.1002/fld

3.2. Phase-field model

Additionally to the previous description of the interface as a sharp hypersurface, so-called diffuse-interface models are used. These models are of growing interest for multiphase flow simulations because they can easily handle topological changes and moving contact lines and allow for a simple surface/bulk coupling of additional soluble species.

Diffuse-interface models account for a partial mixing of the fluids at a small length scale. Therefore, the interface is represented as a thin layer of finite thickness ϵ. An auxiliary phase-field function ϕ is used to indicate the phases. The phase-field function varies smoothly between distinct values in both phases, here $\phi = 1$ in the liquid and $\phi = -1$ in the gas. The interface can be associated with an intermediate level set of the phase-field function (here $\phi = 0$). Diffuse-interface approaches for mixtures of two immiscible, incompressible fluids with matched densities lead to the so-called Model H [17], which has been considered by several authors, see for example, [18–21]. An extension for non-matched densities by [22] leads to:

$$\rho_r(\phi)(\partial_t \mathbf{u} + (\mathbf{u}\cdot\nabla)\mathbf{u}) = -\nabla p + \nabla\cdot\left(\eta_r(\phi)\frac{1}{Re_L}\mathbf{D}(\mathbf{u})\right) + \mathbf{F} + \mu\nabla\phi, \tag{3a}$$

$$\nabla\cdot\mathbf{u} = 0, \tag{3b}$$

$$\partial_t\phi + \mathbf{u}\cdot\nabla\phi = \nabla\cdot(M\nabla\mu), \tag{3c}$$

$$\mu = \frac{3}{2\sqrt{2}}\frac{1}{Re_L Ca}\left(\epsilon^{-1}W'(\phi) - \epsilon\Delta\phi\right). \tag{3d}$$

Here, μ is the chemical potential, M a mobility, the function $W(\phi) = \frac{1}{4}(\phi^2-1)^2$ is a double-well potential, and $\mathbf{D}(\mathbf{u}) = (\nabla\mathbf{u} + (\nabla\mathbf{u})^\top)$. The density and the viscosity ratios ρ_r and η_r, respectively, are defined relative to the density/viscosity in the liquid domain (hence, $\rho_r(+1) = \eta_r(+1) = 1$). We define r to be the density and the viscosity ratio in the gas, which yields $\rho_r(-1) = \eta_r(-1) = r$. Unless otherwise stated, we use the ratio $r = 1/100$.

By using energy methods, a thermodynamically consistent model for non-matched densities is also available and used in EconDrop, see [23, 24]. In particular, the momentum equation differs from (3a):

$$\rho_r(\phi)\partial_t\mathbf{u} + \left(\left(\rho_r(\phi)\mathbf{u} - \rho_r'(\phi)M\nabla\mu\right)\cdot\nabla\right)\mathbf{u} = -\nabla p + \nabla\cdot\left(\eta_r(\phi)\frac{1}{Re_L}\mathbf{D}(\mathbf{u})\right) + \mathbf{F} + \mu\nabla\phi. \tag{4a}$$

For both diffuse-interface models, we choose a mobility $M = k\epsilon$ with a constant factor k. Note, that both models have been shown to approach the sharp-interface model (2a)–(2c) in the limit of vanishing interfacial thickness, $\epsilon \to 0$, if $M = \mathcal{O}(\epsilon)$ [23]. A numerical benchmark comparison of the previous diffuse-interface models with level set and volume of fluid methods has been conducted in [14] and shows good agreement.

4. NUMERICAL METHODS

Four different solvers using different numerical approaches to the capillary problem at hand were used. In the following, we give a short description of each solver. For the 3D rotational symmetric benchmarks, the symmetry was exploited, and a suitable coordinate transformation was used to do the computations in a 2D domain (see Figure 3 for an illustration).

Copyright © 2013 John Wiley & Sons, Ltd.

DOI: 10.1002/fld

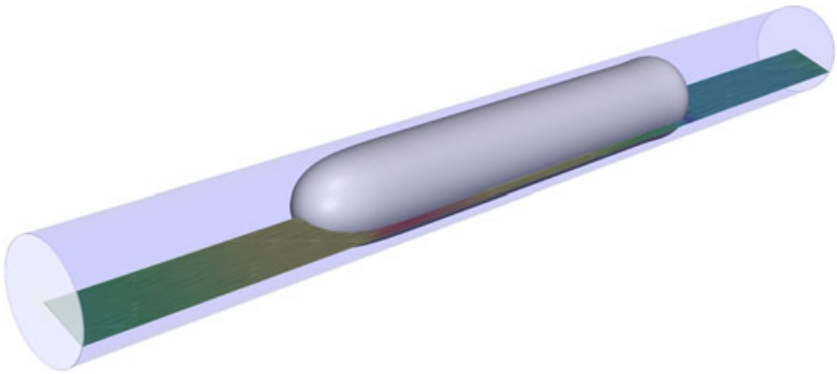

Figure 3. Domain of computation and 3D domain for the rotational symmetric simulations (data from the simulations using NAVIER with data from the experimental setup, color indicates pressure).

4.1. Solvers implementing the sharp-interface model

The two solvers NAVIER and MooNMD use the FEM to implement the sharp-interface model, that is, (2a), (2b), (2d). Both solvers use a mesh that is adapted to the geometry, that is, to the phase boundary. Because the mesh is always aligned with the problem geometry, it moves over time. To make computations in such a setting possible, we use ALE coordinates.

To achieve a very accurate representation of the problem geometry, we use isoparametric elements. This means that especially the curvature can be represented precisely, in particular when using a 'natural' variational formulation of the curvature (from [25]), that is, for (2d), the following finite element formulation is used:

$$-\int_\Gamma \kappa \mathbf{n}\varphi = -\int_\Gamma \underline{\Delta}\varphi = \int_\Gamma \underline{\nabla}\mathrm{id} : \underline{\nabla}\varphi, \tag{5}$$

where φ is a test function, $\underline{\Delta}$ is the Laplace–Beltrami operator, and $\underline{\nabla}$ is the tangential gradient.

In the bulk phase, both solvers use a standard Taylor–Hood element (P^2-elements for the velocity and P^1-elements for pressure). As the computations in the bulk phase have a much less pronounced effect on the simulation compared with the effects close to the phase interface, the mesh is adapted such that only the phase interface is resolved precisely, whereas the bulk equations can be solved with lower numerical costs.

For the Taylor flow simulation, both solvers used the implicit Euler scheme, because its relatively high numerical dissipativity leads to a faster convergence to the stationary state, which is sought for in this situation. The nonlinear implicit equations are solved by a Richardson-type iteration, where each iteration step uses a semi-implicit treatment of the curvature. The semi-implicit treatment of the curvature can be proven to be stable [26].

As initial values, the velocity is set to $\mathbf{u} = 0$ and the pressure difference is initialized as a positive value. The linear systems resulting from the discretization are solved with the direct solver UMFPACK [27], both for NAVIER and for MooNMD.

NAVIER

NAVIER is a solver that specializes in high resolution of capillary flows. Whereas the simulation of coupled systems (e.g., with heat or species transport) is also possible, the main focus is on curvature driven simulations.

Many numerical problems have been handled with NAVIER, most of them are multiphase or capillary problems. Some examples include crystal growth in a floating zone [28], rising droplets

Copyright © 2013 John Wiley & Sons, Ltd.

DOI: 10.1002/fld

in a liquid/liquid extraction system [29], and simulations of liquid/gas phases with mass transfer (evaporation/condensation) [30, 31].

To simulate Taylor flow as compared to single Taylor bubbles, we used a periodic grid in NAVIER (periodic velocity and pressure space), and the external pressure gradient was prescribed as a volume force on the fluid.

All simulations were run on a standard workstation (Intel Xeon CPU, 2.6 GHz, serial execution). Time step sizes were chosen depending on the capillary number. For example, for the 2D example (Problem 1), they were 10^{-1} (for $Ca = 2 \cdot 10^{-1}$) to 10^{-3} (for $Ca = 2 \cdot 10^{-4}$).

The execution times ranged from 20 min to 96 h depending on the film width (lower film widths require finer meshes and time step sizes, which in turn lead to a longer computation time).

MooNMD

MooNMD is a general purpose finite element program package [32]. Its design is highly modular so that it can be easily extended to solve arbitrary PDEs. This package has been successfully applied, for example, in the solution of the steady state and time-dependent incompressible Navier–Stokes equations [33–35], large eddy simulations [36], free boundary value problems with capillary surfaces and ferrofluids [37, 38], multiphase problems with and without surface active agents [39–41], population balance systems [42–44], and convection-diffusion equations by stabilized finite elements [45, 46].

Although the standard Taylor–Hood element is used for the results presented here other inf-sup stable finite elements were possible, for example, the $P^2_{\text{bubble}}/P^1_{\text{disc}}$ pair (continuous piecewise quadratic velocity space enriched with a cubic bubble function on each cell and discontinuous pressure).

A periodic grid is used, but as distinct from NAVIER, only the velocity space consists of periodic functions. The pressure space is left non-periodic; thus, the pressure difference between the top and the bottom of the domain is incorporated as a natural boundary condition. Furthermore, for the pure 2D case (Problem 1), the symmetry of the problem was exploited, computing only on one half (longitudinal) of the original domain.

A fixed time step size was used, which varies from 10^{-4} for the cases $Ca = 2 \cdot 10^{-1}, 2 \cdot 10^{-2}$ and 10^{-5} for $Ca = 2 \cdot 10^{-3}$ to 10^{-6} for the case $Ca = 2 \cdot 10^{-4}$. The simulations were run in serial execution on an Intel Xeon CPU at 2.8 GHz. The computation times vary from 4 to about 96 h depending on film width (see 4.1).

4.2. Solvers implementing the phase-field model

The two diffuse-interface solvers AMDiS and EconDrop were used for this study. In both solvers, adaptive meshes are indispensable for providing a high spatial resolution along the fluid–fluid interface. Whereas the domain away from the interface is discretized with an equidistant mesh of grid size $1/16$, we adapt the grid size at the interface to obtain around 10 degrees of freedom across the interface in the normal direction. The resulting meshes are similar to meshes generated using an L^2-like error indicator based on a jump residual (e.g., [47]). Note that rigorous error estimates in h and ϵ only exist for simpler problems like the Allen–Cahn equation (see [48]).

Periodic boundary conditions are specified for all variables at inflow and outflow boundaries of the domain. Therefore, we induce the pressure difference by applying a volume force $\mathbf{F} = \mathbf{e}_y \Delta p / L$. At the side walls, we impose a no-slip condition for the velocity field $\mathbf{u}$.

A considerable improvement of the simulation speed is achieved by using a moving frame of reference. Because the position of the mesh is then constant with respect to the center of gravity of the bubble, adaptive refinement is much easier to carry out. Therefore, we calculate the bubble velocity $\mathbf{u}_b$ by $\mathbf{u}_b = \left(\int_\Omega (1-\phi)\mathbf{u}\right) / \left(\int_\Omega 1-\phi\right)$ and replace the velocity of the convective terms in Equations (3a) and (3c) by $(\mathbf{u} - \mathbf{u}_b)$.

To improve comparability, we choose equal mobilities in both codes, $M = \epsilon/500$. The volume force $\mathbf{F}$ is updated in every time step: $\mathbf{F}_{new} = \mathbf{F} \cdot |\mathbf{u}_b \cdot \mathbf{e}_y|^{-1}$. Although the pressure difference is

Copyright © 2013 John Wiley & Sons, Ltd.

DOI: 10.1002/fld

unknown *a priori*, we observe very quick convergence towards a constant bubble velocity. As initial values, we take a parabolic profile for the velocity $\mathbf{u}$ and a positive pressure difference.

AMDiS

AMDiS is an adaptive finite element toolbox [49], which is designed for fast implementation of arbitrary PDEs. AMDiS is freely available for research and teaching purposes and can be downloaded at http://www.amdis-fem.org. The software has been used for a wide range of problems, from elasticity in bones [50] to multiphase flows with nanoparticles [51].

The Navier–Stokes Cahn–Hilliard equations (3) were implicitly coupled using the new velocity in Equation (3c) and the new chemical potential in Equation (3a). This results in a stabilization of high surface tensions and allows larger time steps. We use a semi-implicit Euler time stepping algorithm of which we expect to converge fast to the stationary solution due to its high numerical dissipativity. A typical simulation starts with small time steps of 10^{-3}. As the stationary solution is approached, time steps are increased either manually or by a CFL strategy. In the latter case, we stop the simulation if the time step exceeds 10. We discretize in space by a standard Taylor–Hood element for the Navier–Stokes equation with P^2-elements for $\mathbf{u}$, ϕ and μ and P^1-elements for p. To prevent any touching of the wall and the bubble, we impose the Dirichlet boundary condition $\phi = 1$ at the side walls.

We use an MPI-based parallelization with 4–16 cores and a PETSc solver transpose free quasi-minimal residual with the block Jacobi preconditioner. The local subproblems are solved using incomplete LU factorization. For different capillary, numbers considered here result in a different thickness of the liquid film besides the bubble. To resolve this film appropriately, we use in 2D $\epsilon = 0.0075, 0.00375, 0.0015$ for $Ca = 2 \cdot 10^{-1}, 2 \cdot 10^{-2}, 2 \cdot 10^{-3}$, respectively, and $\epsilon = 0.005$ in the 3D simulations. Smaller ϵ goes along with a finer grid, which gives a computational effort of 8 to 48 h for the different simulations.

EconDrop

EconDrop is an adaptive finite element and finite volume framework that focuses on two-phase flow. Typical applications so far are electrowetting simulations [52, 53] and dewetting processes [54].

It is implemented in C++, using the Intel Math Kernel Library, which provides the linear solver PARDISO. The latter is optimized for single-node multicore computations [55]. Because EconDrop has no parallelization so far, mesh refinement and therefore interface thickness is bounded from below because of memory limitations. For the capillary number $Ca = 0.02$, the interface thickness parameter ϵ is twice as large compared with AMDiS.

Touching of the wall and the bubble is prevented by altering the boundary conditions for ϕ according to [52], such that the contact angle between the bubble and wall is zero.

More details about a stable and practicable implementation of the model can be found in [24].

A simple iteration scheme is used to recover the implicit coupling between the momentum Equation (4a) and Cahn–Hilliard Equations (3c) and (3d): we successively solve the 4th order equation, the momentum equations, and the convection part of the CH equation, always using the last updates for ϕ, μ, or $\mathbf{u}$. Starting over in the same time step, we repeat iterating until convergence. In our case, this happens after three to four iterations.

For the discretization in time, we use an implicit Euler scheme, time steps may vary using a CFL strategy or a heuristic argument in case of an almost stationary solution. In space, we use Taylor–Hood elements (P^2 elements only for the velocity $\mathbf{u}$). For the linearized 4th order problem arising from the Cahn–Hilliard equation, we use BiCGstab. For the convective part of (3c), we use a finite volume scheme of second order with Engquist–Osher flux and min-mod limiter [56]. The saddle point problem is solved by Picard iteration.

The simulations were run on a workstation (Intel Xeon CPU, 2.8 GHz, multithreaded execution). Wall time ranges from 24 hours to 7 days, depending on the interface thickness and the resulting mesh size. We resolve the interface by approximately 8–10 DOFs in normal direction. Note that EconDrop is a 2D code (a 3D version of EconDrop is currently under development) and did therefore not take part in the comparison of the 3D axisymmetric test cases.

Copyright © 2013 John Wiley & Sons, Ltd.

DOI: 10.1002/fld

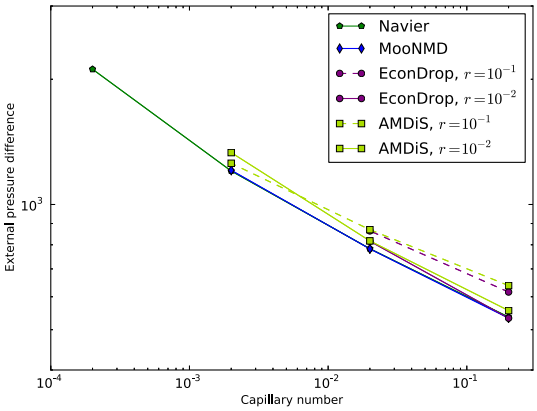

Figure 4. Comparison of computed external pressure difference at different capillary numbers (Problem 1).

5. NUMERICAL RESULTS

5.1. Numerical benchmark in 2D, Problem 1

Comparison of external pressure gradients

The comparison of external pressure gradients needed to achieve a prescribed bubble velocity is somewhat similar to the comparison of bubble rise velocities in other benchmarks [13]. However, as different rise velocities lead to different local Reynolds and capillary numbers, we prescribe the velocity and compare the pressure gradient to achieve this velocity instead. This approach enables us to compare bubble shapes at exactly the same capillary (and Reynolds) number, which would not be possible otherwise.

Figure 4 shows the external pressure difference at different capillary numbers. The diffuse-interface simulations are conducted with two density and viscosity ratios: $r = 1/10$ and $r = 1/100$. Both sharp-interface codes (NAVIER, MooNMD) show excellent agreement. The agreement with the diffuse-interface codes EconDrop and AMDiS is good at the higher density ratio ($r = 1/100$). Only for $Ca = 0.002$ does the result from AMDiS diverge from the sharp-interface results for decreasing density ratio. This indicates that the interface thickness ϵ is still not fine enough to yield the results of the sharp-interface models. Because the sharp-interface codes do not model the interior of the boundary, their approach corresponds to a very high density ratio (the viscosity ratio has only small effects in this kind of experiment [3]).

Comparison of velocity profiles

For the comparison of velocity profiles, the computed flow field was evaluated at the y-position of the rear of the bubble. Both velocity components are plotted in Figure 5. The overall agreement of the results is quite good. The deviation of the EconDrop results from the other codes is a little higher, most probably because of the larger interface thickness and coarser mesh used in these simulations.

Comparison of film widths

For the comparison of film widths, the distance of the bubble boundary to the wall was computed and averaged in vertical direction over a distance of 1 hydraulic diameter from the bubble center. In the sharp-interface codes, the bubble boundary is explicitly given, whereas in diffuse-interface models, it is implicitly defined as the level set $\phi = 0$.

The resulting film widths are plotted in Figure 6. For the diffuse-interface codes, only the values from the runs with a high density ratio $r = 1/100$ were used. The approximation formulas from Bretherton (1a) and Halpern/Gaver (1b) were also included in the plot, for comparison. Solid lines were used in the range of capillary numbers specified as valid for the approximation by the original authors.

Copyright © 2013 John Wiley & Sons, Ltd.

DOI: 10.1002/fld

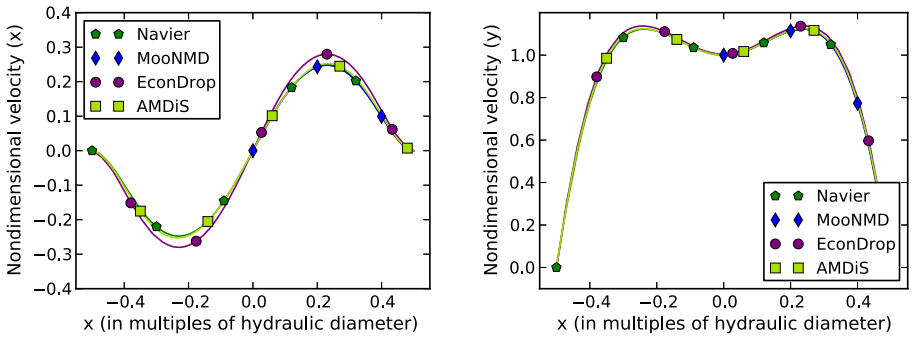

Figure 5. Comparison of the x-component (left) and y-component (right) of the velocity at a cut directly below the bubble (Problem 1).

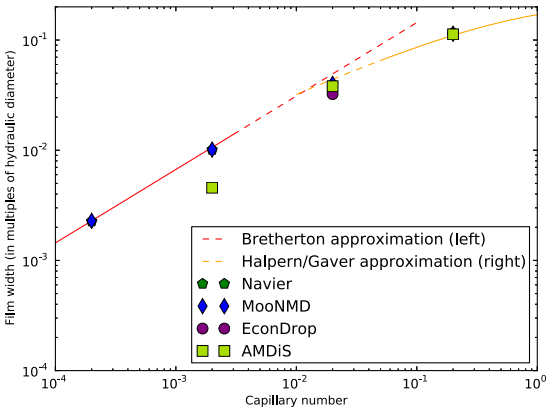

Figure 6. Comparison of film width of a Taylor bubble with two approximation formulas from literature for different capillary numbers (Problem 1).

The simulation results are in good accordance with the given formulas. For lower capillary numbers, the smaller lower film width is harder to resolve with the diffuse-interface models, because it requires a computationally expensive small interface thickness ε. Therefore, EconDrop gives no comparable result for $Ca = 2 \cdot 10^{-3}$ and smaller. Because of its highly effective parallelization, AMDiS can yield a result for $Ca = 2 \cdot 10^{-3}$, but it clearly deviates from the results of the sharp-interface models, because the interface thickness is still not small enough to accurately resolve the thin liquid film surrounding the bubble.

Comparison of bubble shape

In Figure 7, an overview of the computed bubble shape is given for all four solvers. As an example, we chose a medium capillary number $Ca = 2 \cdot 10^{-2}$, as this is closest to physical values (see Section 2). In all four simulations, the typical bullet shape of a Taylor bubble can be seen.

In Figure 8, close-up views of the cap and the rear of the bubbles can be seen. At the cap, all simulations are in perfect agreement, whereas at the rear, EconDrop shows a less pronounced bullet shape compared with the other codes. This might be induced by the differing boundary condition, which does not explicitly prescribe a pure phase at the boundary but allows for free movement of the diffuse interface.

5.2. Rotational symmetric benchmark in 3D, Problem 2

Comparison of external pressure gradients

Just as for Problem 1, the external pressure gradients were compared for varying capillary numbers (Figure 9).

Copyright © 2013 John Wiley & Sons, Ltd.

DOI: 10.1002/fld

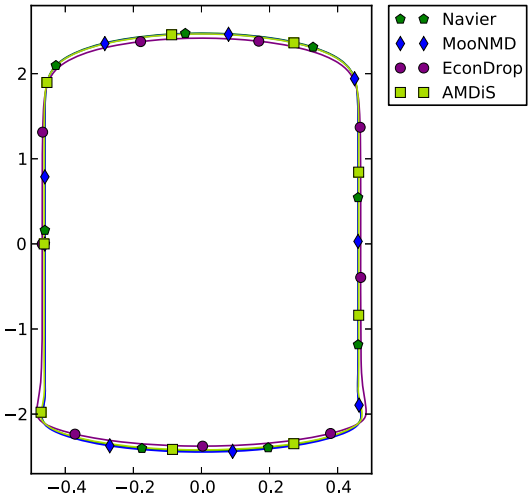

Figure 7. Comparison of bubble shape: overview over the complete bubble (Problem 1).

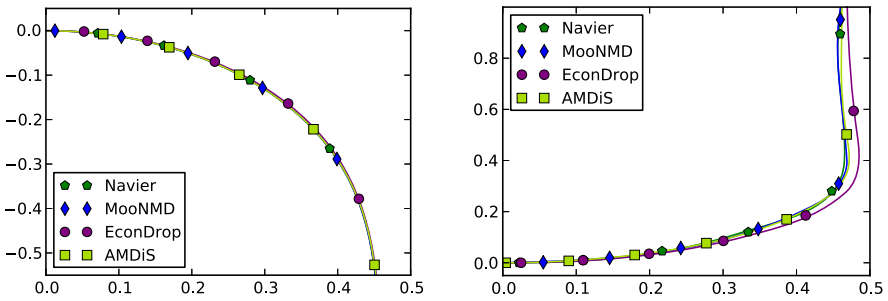

Figure 8. Comparison of bubble shape: close up at cap and rear of the bubble (Problem 1).

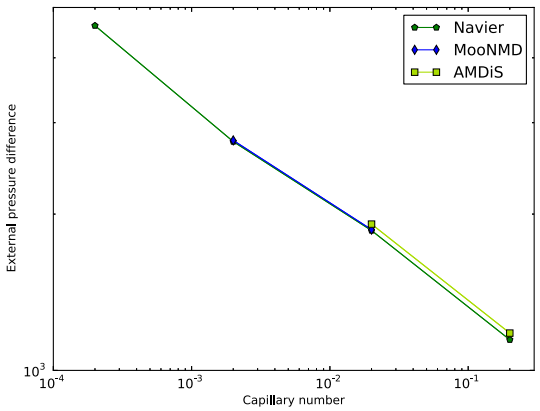

Figure 9. Comparison of computed external pressure difference at different capillary numbers (Problem 2).

The results are qualitatively very similar to the pure 2D results. As before, the agreement of the sharp-interface codes is excellent, and the diffuse-interface code AMDiS is also very close to the sharp-interface results.

Comparison of velocity profiles

The velocity profiles were compared exactly as in Problem 1. The results are plotted in Figure 10. The overall agreement is as good as in the 2D case.

Copyright © 2013 John Wiley & Sons, Ltd.

DOI: 10.1002/fld

Comparison of film widths

The approximation formula (1a) was originally developed for film widths in an axisymmetric setup [11]. Usually, it is also used for 2D simulations (e.g., in [3]). For higher capillary numbers, the approximation formula (1b) was developed for a 2D scenario. Because this formula gives a reasonable approximation also in the rotational symmetric 3D case, we used it as an initial guess for the film width in our simulations. Figure 11 shows that both approximation formulas work equally well in an axisymmetric 3D setup.

The film widths were computed in the same way as in Section 5.1.

Comparison of bubble shape

The shapes of the bubbles are shown in Figures 12 and 13. Again, we present the result for $Ca = 2 \cdot 10^{-2}$. As in the 2D case, the semi-analytical predictions from Bretherton and Halpern/Gaver, respectively, are in good accordance with the simulation data.

5.3. Comparison to experimental data in 3D, problem 3

Comparison of bubble shape

For comparison with experimental results, only the bubble shape measured in radiographic projection was available. Figure 14 shows an overview of the whole bubble domain (2D section of 3D axisymmetric bubble), and Figure 15 shows close-up views at the cap and the rear of the bubble. Whereas the numerical results are in good accordance, the bullet shape seems to be less pronounced in the experimental results, that is, the numerical results exhibit too low surface tension effects. It remains unclear whether this is due to some error in the measurement (e.g., by a violation of the

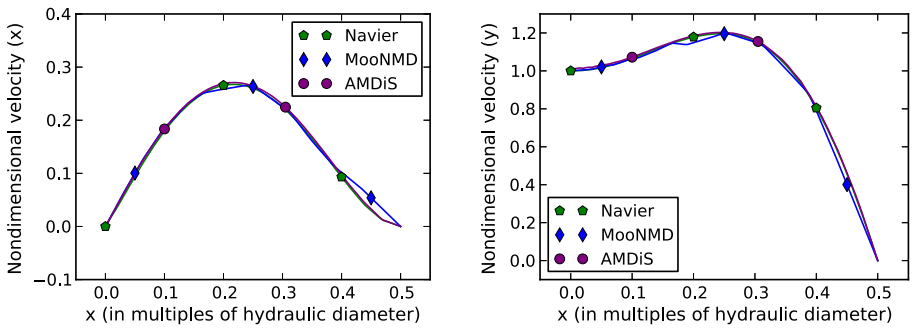

Figure 10. Comparison of the x-component (left) and y-component (right) of the velocity at a cut directly below the bubble (Problem 2).

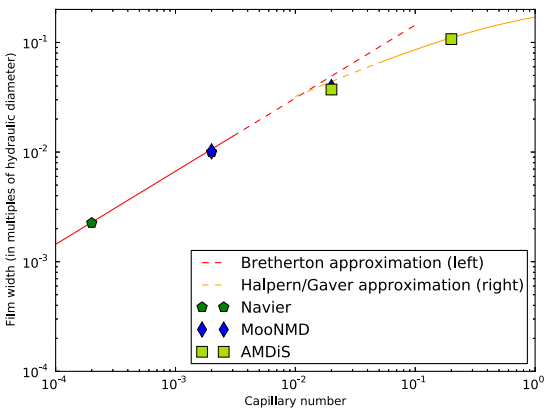

Figure 11. Comparison of film width of a Taylor bubble with two approximation formulas from literature for different capillary numbers (Problem 2).

Copyright © 2013 John Wiley & Sons, Ltd.

DOI: 10.1002/fld

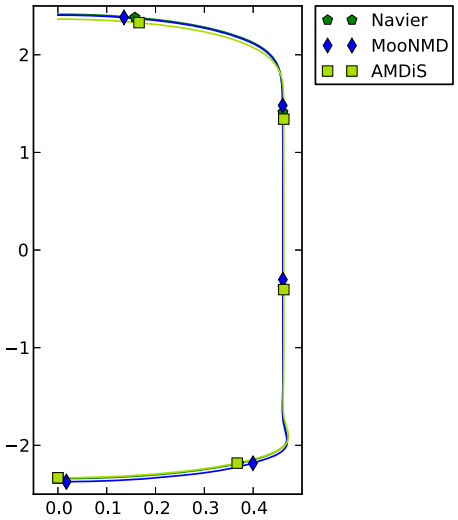

Figure 12. Comparison of bubble shape: overview of the complete bubble (Problem 2).

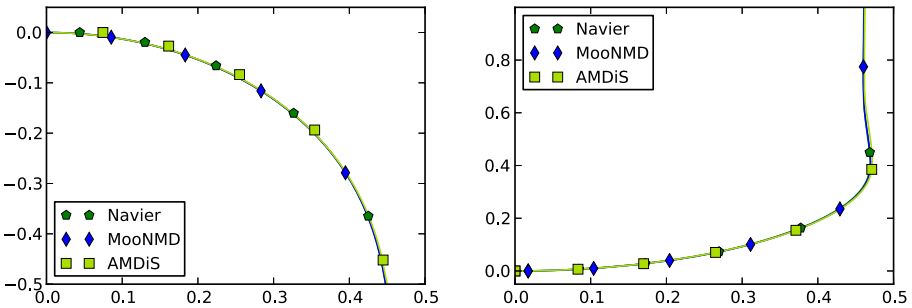

Figure 13. Comparison of bubble shape: close up at cap and rear of the bubble (Problem 2).

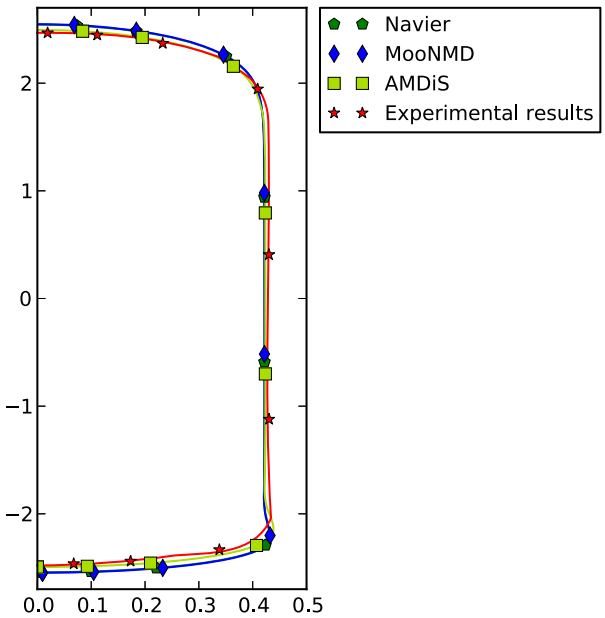

Figure 14. Comparison of bubble shape: overview over the complete bubble (Problem 3).

Copyright © 2013 John Wiley & Sons, Ltd.

DOI: 10.1002/fld

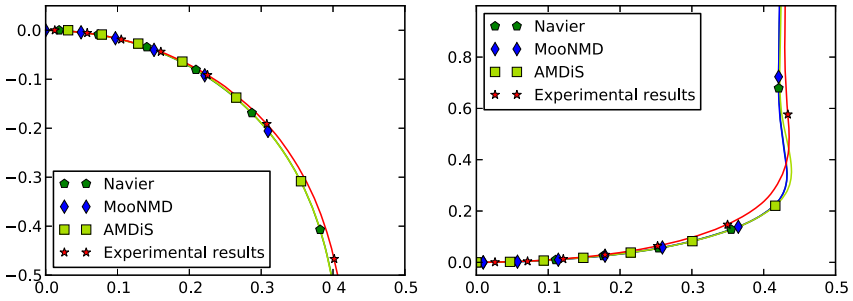

Figure 15. Comparison of bubble shape: close up at cap and rear of the bubble (Problem 3).

assumption of rotational symmetry, wrong physical parameters, etc.), or to some unknown physical effects. The whole bubble shape is however well-reproduced in the numerical simulations.

6. CONCLUSION

We compared different implementations of both sharp and diffuse-interface models for Taylor flow. The present results affirm the applicability and the usability of both kinds of models for a physically relevant parameter regime. Although the models are conceptually very different, the results are in good accordance, also when compared with experimental data. A mesh aligned to the problem domain, that is the bubble, is advantageous for very small capillary numbers. In this case, a very fine film width needs to be resolved, which can be performed easier with an explicit representation of the grid. Even when highly parallelized, diffuse-interface models cannot give valuable results for $Ca < 2 \cdot 10^{-3}$. On the other hand, large deformations of the computational domain can be handled better with an implicit representation of the interface. Therefore, diffuse-interface models may be favorable for higher capillary numbers and even allow more complex scenarios such as drop coalescence or separation.

Furthermore, the approximation formulas for the film width of Bretherton [11] and Halpern and Gaver [12] could be confirmed by all models even in a 3D axisymmetric test scenario.

The present results can form a basis for further numerical studies of more complex examples of Taylor flow, for example, flow containing soluble surfactants, flow with mass transfer, or the dissolution of a gaseous bubble.

ACKNOWLEDGEMENTS

This work has been supported by Deutsche Forschungsgemeinschaft in the Priority Programme 1506 'Transport processes at fluidic interfaces'. We kindly acknowledge the provision of beamtime by the synchrotron radiation source ANKA, and we acknowledge the kind support by T. Rolo during the operation of the TOPO/TOMO beamline, which is directed by Prof. T. Baumbach, KIT.

REFERENCES

1. Davies RM, Taylor G. The mechanics of large bubbles rising through extended liquids and through liquids in tubes. *Proceedings of the Royal Society of London. Series A, Mathematical and Physical Sciences* 1950; **200**(1062):375–390. DOI: 10.1098/rspa.1950.0023.
2. Thulasidas T, Abraham M, Cerro R. Bubble-train flow in capillaries of circular and square cross section. *Chemical Engineering Science* 1995; **50**(2):183–199. DOI: 10.1016/0009-2509(94)00225-G.
3. Öztaskin M., Wörner M., Soyhan H. S. Numerical investigation of the stability of bubble train flow in a square minichannel. *Physics of Fluids* 2009; **21**(4):042108-1–042108-17. DOI: 10.1063/1.3101146.
4. Lu X, Prosperetti A. Axial stability of Taylor bubbles. *Journal of Fluid Mechanics* 2006; **568**:173–192. DOI: 10.1017/S0022112006002205.
5. Kreutzer MT, Kapteijn F, Moulijn JA, Heiszwolf JJ. Multiphase monolith reactors: chemical reaction engineering of segmented flow in microchannels. *Chemical Engineering Science* 2005; **60**(22):5895–5916. DOI: 10.1016/j.ces.2005.03.022.

Copyright © 2013 John Wiley & Sons, Ltd.

6. Reinecke N, Mewes D. Oscillatory transient two-phase flows in single channels with reference to monolithic catalyst supports. *International Journal of Multiphase Flow* 1999; **25**(6-7):1373–1393. DOI: 10.1016/S0301-9322(99)00046-4.
7. Williams JL. Cheminform abstract: monolith structures, materials, properties and uses. *ChemInform* 2002; **33**(11):3–39. DOI: 10.1002/chin.200211225.
8. Roy S, Bauer T, Al-Dahhan M, Lehner P, Turek T. Monoliths as multiphase reactors: a review. *AIChE Journal* 2004; **50**(11):2918–2938. DOI: 10.1002/aic.10268.
9. Günther A, Jhunjhunwala M, Thalmann M, Schmidt MA, Jensen KF. Micromixing of miscible liquids in segmented gas-liquid flow. *Langmuir* 2005; **21**(4):1547–1555. DOI: 10.1021/la0482406.
10. Muradoglu M, Günther A, Stone HA. A computational study of axial dispersion in segmented gas-liquid flow. *Physics of Fluids* 2007; **19**(7):072109-1–072109-11. DOI: 10.1063/1.2750295.
11. Bretherton FP. The motion of long bubbles in tubes. *Journal of Fluid Mechanics* 1961; **10**(166). DOI: 10.1017/S0022112061000160.
12. Halpern D, Gaver P. Boundary element analysis of the time-dependent motion of a semi-infinite bubble in a channel. *Journal of Computational Physics* 1994; **115**(366). DOI: 10.1006/jcph.1994.1202.
13. Hysing S, Turek S, Kuzmin D, Parolini N, Ganesan E, Burmanand S, Tobiska L. Quantitative benchmark computations of two-dimensional bubble dynamics. *International Journal for Numerical Methods in Fluids* 2008; **60**:1259–1288. DOI: 10.1002/fld.1934.
14. Aland S, Voigt A. Benchmark computations of diffuse interface models for two-dimensional bubble dynamics. *International Journal for Numerical Methods in Fluids* 2012; **69**:747–761. DOI: 10.1002/fld.2611.
15. Rack A, Weitkamp T, Bauer Trabelsi S, Modregger P, Cecilia A, dos Santos Rolo T, Rack T, Haas D, Simon R, Heldele R, Schulz M, Mayzel B, Danilewsky AN, Waterstradt T, Diete W, Riesemeier H, Müller BR, Baumbach T. The micro-imaging station of the topotomo beamline at the anka synchrotron light source. *Nuclear Instruments and Methods in Physics Research Section B: Beam Interactions with Materials and Atoms* 2009; **267**(11):1978–1988. DOI: 10.1016/j.nimb.2009.04.002.
16. Gallant RW. Physical properties of hydrocarbons.14.propylene glycols and glycerine. *Hydrocarbon Processing* 1967; **46**(5):201–215.
17. Hohenberg PC, Halperin BI. Theory of dynamic critical phenomena. *Reviews of Modern Physics* 1977 Jul; **49**:435–479. DOI: 10.1103/RevModPhys.49.435.
18. Anderson D, McFadden G, Wheeler A. Diffuse-interface methods in fluid mechanics. *Annual Review of Fluid Mechanics* 1998; **30**:139–165. DOI: 10.1146/annurev.fluid.30.1.139.
19. Jaqmin D. Calculation of two-phase Navier-Stokes flows using phase-field modelling. *Journal of Computational Physics* 1999; **155**:96–127. DOI: 10.1006/jcph.1999.6332.
20. Feng X. Fully discrete finite element approximations of the Navier–Stokes–Cahn-Hilliard diffuse interface model for two-phase fluid flows. *SIAM Journal on Numerical Analysis* 2006; **44**:1049–1072. DOI: 10.1137/050638333.
21. Kay D, Welford R. Efficient numerical solution of Cahn-Hilliard-Navier-Stokes fluids in 2d. *SIAM Journal on Scientific Computing* 2007; **29**:15–43. DOI: 10.1137/050648110.
22. Ding H, Spelt PD, Shu C. Diffuse interface model for incompressible two-phase flows with large density ratios. *Journal of Computational Physics* 2007; **226**:2078–2095. DOI: 10.1016/j.jcp.2007.06.028.
23. Abels H, Garcke H, Grün G. Thermodynamically consistent, frame indifferent diffuse interface models for incompressible two-phase flows with different densities. *Mathematical Models and Methods in Applied Sciences* 2012; **22**(3):1150013-1–1150013-40. DOI: 10.1142/S0218202511500138.
24. Grün G, Klingbeil F. Two-phase flow with mass density contrast: stable schemes for a thermodynamic consistent and frame-indifferent diffuse-interface model. *ArXiv e-prints* 2012. DOI: arXiv:1210.5088.
25. Dziuk G. An algorithm for evolutionary surfaces. *Numerische Mathematik* 1991; **58**:603–611. DOI: 10.1007/BF01385643.
26. Bänsch E. Finite element discretization of the Navier-Stokes equations with a free capillary surface. *Numerische Mathematik* 2001; **88**:203–235. DOI: 10.1007/PL00005443.
27. Davis TA. Algorithm 832: UMFPACK v4.3—an unsymmetric-pattern multifrontal method. *ACM Transactions on Mathematical Software* 2004; **30**(2):196–199. DOI: 10.1145/992200.992206.
28. Bänsch E, Höhn B. Numerical simulation of a silicon floating zone with a free capillary surface. In *Proceedings of the SCCE II*, Vol. 1. Springer: Berlin Heidelberg, 1999; 328–335.
29. Bäumler K., Wegener M., Paschedag A. R., Bänsch E. Drop rise velocities and fluid dynamic behavior in standard test systems for liquid/liquid extraction–experimental and numerical investigations. *Chemical Engineering Science* 2011; **66**(3):426–439. DOI: 10.1016/j.ces.2010.11.009.
30. Krahl R, Gerstmann J. Non-isothermal reorientation of a liquid surface in an annular gap. In **4**$^{\text{th}}$ *International Berlin Workshop – IBW 4 on Transport Phenomena with Moving Boundaries*, Schindler FP (ed.), Fortschritt-Berichte VDI, Reihe 3: Verfahrenstechnik. VDI-Verlag: Düsseldorf, 2007; 227–241.
31. Krahl R, Gerstmann J, Behruzi P, Bänsch E, Dreyer ME. Dependency of the apparent contact angle on nonisothermal conditions. *Physics of Fluids* 2008; **20**(4):042101-1–042101-14. DOI: 10.1063/1.2899641.
32. John V, Matthies G. MooNMD a program package based on mapped finite element methods. *Computing and Visualization in Science* 2004; **6**:163–170. DOI: 10.1007/s00791-003-0120-1.
33. John V. Reference values for drag and lift of a two-dimensional time-dependent flow around a cylinder. *International Journal for Numerical Methods in Fluids* 2004; **44**(7):777–788. DOI: 10.1002/fld.679.

Copyright © 2013 John Wiley & Sons, Ltd.

34. John V. Higher order finite element methods and multigrid solvers in a benchmark problem for the 3D Navier-Stokes equations. *International Journal for Numerical Methods in Fluids* 2002; **40**(6):775–798. DOI: 10.1002/fld.377.
35. John V, Matthies G. Higher-order finite element discretizations in a benchmark problem for incompressible flows. *International Journal for Numerical Methods in Fluids* 2001; **37**(8):885–903. DOI: 10.1002/fld.195.
36. Iliescu T, John V, Layton W, Matthies G, Tobiska L. A numerical study of a class of les models. *International Journal of Computational Fluid Dynamics* 2003; **17**(1):75–85. DOI: 10.1080/1061856021000009209.
37. Lavrova O, Matthies G, Mitkova T, Polevikov V, Tobiska L. Finite element methods for coupled problems in ferrohydrodynamics. In *Challenges in Scientific Computing - CISC 2002*, Vol. 35, Bänsch E, Barth TJ, Griebel M, Keyes DE, Nieminen RM, Roose D, Schlick T (eds), Lecture Notes in Computational Science and Engineering. Springer: Berlin Heidelberg, 2003; 160–183, DOI: 10.1007/978-3-642-19014-8_8.
38. Gollwitzer C, Matthies G, Richter R, Rehberg I, Tobiska L. The surface topography of a magnetic fluid – a quantitative comparison between experiment and numerical simulation. *Journal of Fluid Mechanics* 2007; **571**:455–474.
39. Hysing S, Turek S, Kuzmin D, Parolini N, Burman E, Ganesan S, Tobiska L. Quantitative benchmark computations of two-dimensional bubble dynamics. *International Journal for Numerical Methods in Fluids* 2009; **60**(11):1259–1288. DOI: 10.1002/fld.1934.
40. Ganesan S, Tobiska L. A coupled arbitrary Lagrangian–Eulerian and Lagrangian method for computation of free surface flows with insoluble surfactants. *Journal of Computational Physics* 2009; **228**(8):2859–2873. DOI: 10.1016/j.jcp.2008.12.035.
41. Ganesan S, Tobiska L. Arbitrary Lagrangian–Eulerian finite-element method for computation of two-phase flows with soluble surfactants. *Journal of Computational Physics* 2012; **231**(9):3685–3702. DOI: 10.1016/j.jcp.2012.01.018.
42. John V, Mitkova T, Roland M, Sundmacher K, Tobiska L, Voigt A. Simulations of population balance systems with one internal coordinate using finite element methods. *Chemical Engineering Science* 2009; **64**(4):733–741. DOI: 10.1016/j.ces.2008.05.004. 3rd International Conference on Population Balance Modelling.
43. Ganesan S, Tobiska L. An operator-splitting finite element method for the efficient parallel solution of multi-dimensional population balance systems. *Chemical Engineering Science* 2012; **69**:59–68.
44. Krasnyk M, Mangold M, Ganesan S, Tobiska L. Numerical reduction of a crystallizer model with internal and external coordinates by proper orthogonal decomposition. *Chemical Engineering Science* 2012; **70**(0):77 –86. DOI: 10.1016/j.ces.2011.05.053. 4th International Conference on Population Balance Modeling.
45. Ahmed N, Matthies G, Tobiska L, Xie H. Discontinuous Galerkin time stepping with local projection stabilization for transient convection–diffusion-reaction problems. *Computer Methods in Applied Mechanics and Engineering* 2011; **200**(21-22):1747–1756. DOI: 10.1016/j.cma.2011.02.003.
46. Matthies G, Tobiska L. A two-level local projection stabilisation on uniformly refined triangular meshes. *Numerical Algorithms* 2012; **61**:465–478. DOI: 10.1007/s11075-012-9543-4.
47. Verfürth R. In *A review of a posteriori error estimation and adaptive mesh-refinement techniques*, Vol. VI, Teubner BG (ed.), Wiley-Teubner Series Advances in Numerical Mathematics. John Wiley & Sons: Chichester, Stuttgart, 1996; 127 pp.
48. Feng X, Wu Hj. A posteriori error estimates and an adaptive finite element method for the Allen-Cahn equation and the mean curvature flow. *Journal of Scientific Computing* 2005; **24**:121–146. DOI: 10.1007/s10915-004-4610-1.
49. Vey S, Voigt A. AMDiS: adaptive multidimensional simulations. *Computing and Visualization in Science* 2007; **10**(1):57–67. DOI: 10.1007/s00791-006-0048-3.
50. Aland S, Landsberg C, Müller R., Stenger F., Bobeth M., Langheinrich A. C., Voigt A. Adaptive diffuse domain approach for calculating mechanically induced deformation of trabecular bone. *Computer Methods in Biomechanics and Biomedical Engineering* published online 2012. DOI: 10.1080/10255842.2012.654606.
51. Aland S, Lowengrub J, Voigt A. A continuum model of colloid-stabilized interfaces. *Physics of Fluids* 2011; **23**(6):062103. DOI: 10.1063/1.3584815.
52. Eck C, Fontelos M, Grün G, Klingbeil F, Vantzos O. On a phase-field model for electrowetting. *Interfaces Free Bound* 2009; **11**(2):259–290. DOI: 10.4171/IFB/211.
53. Campillo-Funollet E, Grün G, Klingbeil F. On modeling and simulation of electrokinetic phenomena in two-phase flow with general mass densities. *SIAM Journal on Applied Mathematics* 2012; **72**(6):1899–1925. DOI: 10.1137/120861333.
54. Grün G, Mecke K, Rauscher M. Thin-film flow influenced by thermal noise. *Journal of Statistical Physics* 2006; **122**(6):1261–1291. DOI: 10.1007/s10955-006-9028-8.
55. Schenk O, Gärtner K. Solving unsymmetric sparse systems of linear equations with PARDISO. *Future Generation Computer Systems* 2004; **20**:475–487. DOI: 10.1016/j.future.2003.07.011.
56. Kröner D. *Numerical Schemes for Conservation Laws*, Wiley-Teubner Series Advances in Numerical Mathematics. John Wiley & Sons Ltd.: Chichester, Stuttgart, 1997.

Copyright © 2013 John Wiley & Sons, Ltd.